

THREE-DIMENSIONAL VERIFICATION OF INTRACRANIAL TARGET POINT DEVIATION USING MRI-BASED POLYMER-GEL DOSIMETRY FOR CONVENTIONAL AND FRACTIONATED STEREOTACTIC RADIOSURGERY

Kyung-Nam Lee^{*,†}, Dong-Joon Lee[†], and Tae-Suk Suh^{*,†}

^{*}Department of Biomedical Engineering, College of Medicine, The Catholic University of Korea, Seoul 137-701, Korea

[†]Research Institute of Biomedical Engineering, College of Medicine, The Catholic University of Korea, Seoul 137-701, Korea

[‡]Department of Neurosurgery, Ilsanpaik Hospital, College of Medicine, Inje University, Gyeonggi-do 411-706, Korea

Received February 15, 2011 / 1st Revised July 12, 2011 / Accepted for Publication July 13, 2011

Conventional (SRS) and fractionated (FSRS) stereotactic radiosurgery necessarily require stringent overall target point accuracy and precision. We determine three-dimensional intracranial target point deviations (TPDs) in a whole treatment procedure using magnetic resonance image (MRI)-based polymer-gel dosimetry, and suggest a technique for overall system tests. TPDs were measured using a custom-made head phantom and gel dosimetry. We calculated TPDs using a treatment planning system. Then, we compared TPDs using mid bi-plane and three-dimensional volume methods with spherical and elliptical targets to determine their inherent analysis errors; finally, we analyzed regional TPDs using the latter method. Average and maximum additive errors for ellipses were 0.62 and 0.69 mm, respectively. Total displacements were 0.92 ± 0.25 and 0.77 ± 0.15 mm for virtual SRS and FSRS, respectively. Average TPD_{total} at peripheral regions was greater than that at central regions for both. Overall system accuracy was similar to that reported previously. Our technique could be used as an overall system accuracy test that considers the real radiation field shape.

Keywords: Radiosurgery, Overall system test, Target point deviation, Polymer gel, MRI

1. INTRODUCTION

Stereotactic radiosurgery (SRS) is a high precision single dose radiotherapy used to treat various brain abnormalities [1–3]. It has mainly been limited to small focal targets to maintain steep dose fall-off. The amount of irradiated normal tissue increases with target volume. Tolerable dose and target volume for single-fraction irradiation are inversely related [4]. Generally, tissue tolerance limits SRS applications to small targets. Larger brain tumors are treated by conventional fractionated radiotherapy.

Fractionated SRS (FSRS) combines SRS and conventional fractionated radiotherapy and involves both neurosurgical and radiotherapeutic treatments: small daily

doses, as in conventional radiotherapy, and sharp dose gradients, as in SRS, are administered. Because fractionation affects normal brain parenchyma minimally, it allows higher dose delivery with larger margins than those in SRS for normal tissue within treatment volume [5,6]. This is particularly advantageous for lesions near sensitive structures.

SRS and FSRS enable high-accuracy target-volume localization and dose application, high conformity of dose distribution with target volume, and steep dose gradient on target edges. This necessitates high spatial accuracy for target-volume localization and irradiation. Therefore, high target-point accuracy is essential in quality assurance (QA) systems for SRS and FSRS [7–9]. However, factors such as target localization, patient positioning, and mechanical accuracy limit the target-point accuracy, and these cumulatively affect overall TPD. Consequently, overall TPD is more important than

Corresponding author : Dong-Joon Lee, djlee@paik.ac.kr

Tae Suk Suh, suhsanta@catholic.ac.kr

#2240, Daehwa-dong, Ilsanseo-gu, Gyeonggi-do 411-706, Korea

a specific one. System integration tests have been used to measure overall stereotactic target-point accuracy using a film [10–13].

Usually, a bi-planar film embedded between inserts in a phantom is fixed parallel to a pair of mid-planes of the stereotactic coordinate system. After imaging and planning, the phantom is adjusted as for real patient positioning and irradiated using several non-coplanar arcs and a cone collimator. The geometric radiation field center, assumed to be an ideal sphere, dyed on the films is evaluated. However, the field is more likely elliptical because of non-coplanar arcs with a limited combination of gantry and couch angles, mechanical isocenter deviation, and inhomogeneous materials in the phantom. Analysis errors increase with ellipticity of radiation field geometry. Therefore, target-point verification considering the real radiation field shape is required to minimize additional errors. This requires two mid-planes along with additional planes including geometric and spatial information about the radiation field. Three-dimensional information reduces unnecessary analysis errors resulting from deviation of the radiation field shape from an ideal sphere. Three-dimensional measurements using a two-dimensional dosimeter should preferably be avoided because of additional errors and work involved in modifying and installing these detectors. Polymer-gel dosimeters have been used for verifying the three-dimensional dose distribution for SRS [14–17]. These can measure the radiation field relatively accurately using a three-dimensional coordinate system.

The purpose of this study is to verify the three-dimensional target point deviation generated by a whole treatment process using MRI-based gel dosimetry, and to propose our analytical method as a global system accuracy test. For this purpose, we simulated an entire treatment procedure, from imaging to irradiation, based on a radiation treatment plan, using a custom-made anatomical phantom to imitate a variety of small brain lesions in the brain simultaneously.

2. METHODS AND MATERIALS

2.1. Experimental

Overall TPDs were evaluated using a custom-made anthropomorphic head phantom and polymer-gel dosimeter to simulate various brain regions simultaneously. Computerized tomography (CT) scan data was transferred to the treatment planning system. Planning included creating virtual organs-at-risk (OARs). T₂-weighted MR scan was conducted. We calculated TPDs using BrainSCANTM (Version 5.31, BrainLAB, Heimstetten,

Germany). TPDs were compared using mid bi-plane and three-dimensional volume methods for spherical and elliptical targets. TPD was also analyzed using the latter. Figure 1 shows the experimental procedure.

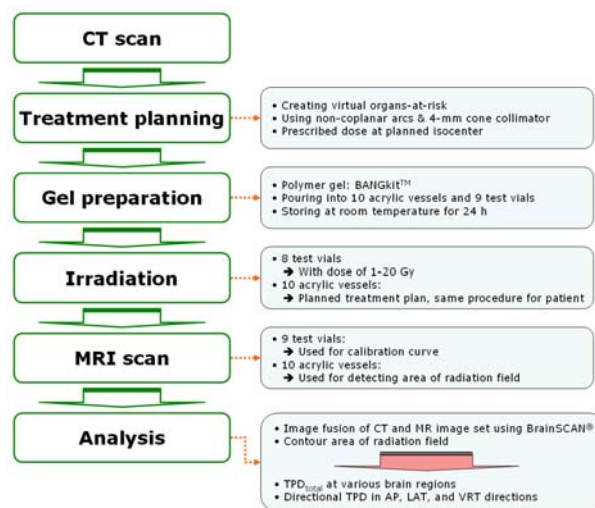


Fig. 1. Experimental procedure.

2.2. Head phantom

The phantom comprises several components (Figure 2). The acrylic vessel contains polymer gel or water, and it has a small hole in the ceiling to control the flows of these liquids using an injector. The position rod defines the vessel position in the phantom. The holder immobilizes other elements, prevents water leakage within the phantom, and enables reproducible positioning of gel dosimeters inside the phantom. It has a positioning plate with 10 holes to represent various brain regions. The shell is filled with water before sealing. It can effectively simulate a patient's head with tumors for virtual treatments.

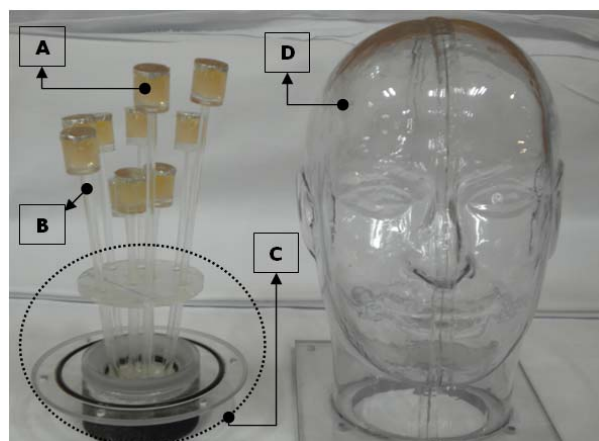


Fig. 2. Custom-made head phantom. Components: A, acrylic vessel; B, position rod; C, fixation holder; D, head-shaped plastic shell.

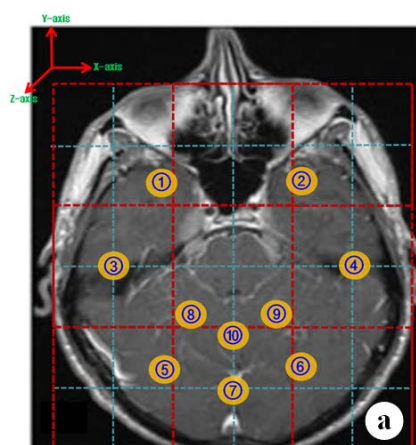


Figure 3A

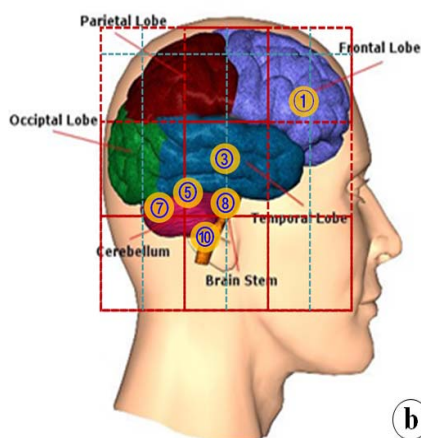


Figure 3B

Fig. 3. Assignment of target numbers. (A, B) Top and side views, respectively, of relative target positions on anatomical image. 1 and 2, 3 and 4, 5–7, and 8–10 correspond to frontal, temporal, cerebellum, and peri-brainstem regions.

2.3. Gel preparation

BANGkitTM (MGS Research Inc., CT, USA) gel comprises gelatin, methacrylic acid, and water, and it is fully oxygenated. It does not respond to radiation unless it is de-oxygenated using ascorbic acid as an oxygen scavenger and copper sulfate catalyst. BANGkitTM is advantageous because it can be manufactured on-demand and container shape can be changed easily [18].

The gel was prepared according to literature [18]. It was poured into 10 acrylic vessels and 9 test vials having outer diameter, length, and wall thickness of 20 and 16, 25 and 110, and 2 and 1.5 mm, respectively. These were stored at room temperature ($\sim 18^{\circ}\text{C}$) in the dark for 24 h. For consistency, gels were always stored together except during scanning and treatment.

2.4. Treatment planning and irradiation

The 10 vessels were positioned in the phantom to represent anatomical regions. The targets were frontal, temporal, peri-brainstem, and cerebellum regions (Figure 3).

For stereotactic CT, a BrainLAB[®] stereotactic localizer box (BrainLAB, Heimstetten, Germany) was attached to the phantom. The phantom was scanned at 0.33-mm slice thickness and $0.69 \times 0.69 \text{ mm}^2$ pixel size using SOMATOM[®] (Siemens, Heidelberg, Germany). Two CT scans were obtained, with the phantom respectively immobilized in a BrainLAB[®] invasive head frame and non-invasive mask frame (BrainLAB, Heimstetten, Germany). For the stereotactic approach, stereotactic coordinate system defined by the stereotactic localizer was transformed to CT coordinate system using BrainSCANTM. All CT data points could then be expressed in stereotactic coordinates.

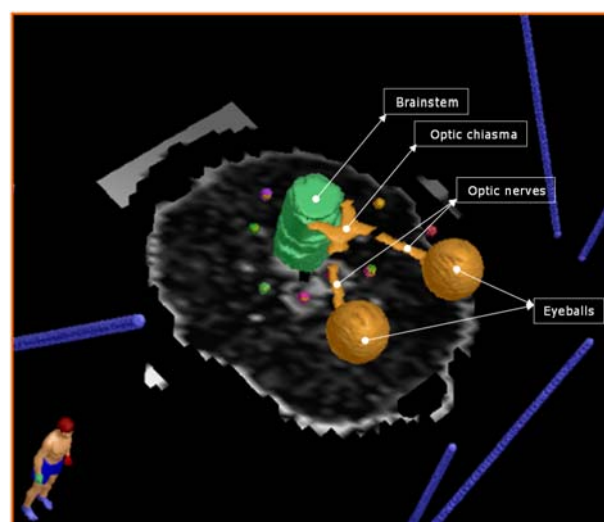


Fig. 4. OARs created during treatment planning: optic nerves, chiasma, eyeballs, and brainstem.

After importing CT images into this system, various OARs were outlined in the CT image set (Figure 4). One isocenter was placed in each acrylic vessel in BrainSCANTM. The maximum dose to the isocenter for SRS and FSRS was 16 and 10 Gy, respectively, using six non-coplanar arcs and a 4-mm cone collimator. All combinations of gantry and couch angles were determined considering the OAR positions to protect them and deliver each prescribed dose to the isocenter.

Before irradiation, a Winston–Lutz test was performed to establish overall rotational characteristics of mechanical isocenter deviation for various combinations of angles. Our system was found suitable for virtual treatments with average isocenter deviation of 0.56 mm.

Before treatment, 8 vials were irradiated at 20°C to obtain a calibration curve; 1 vial was used for back

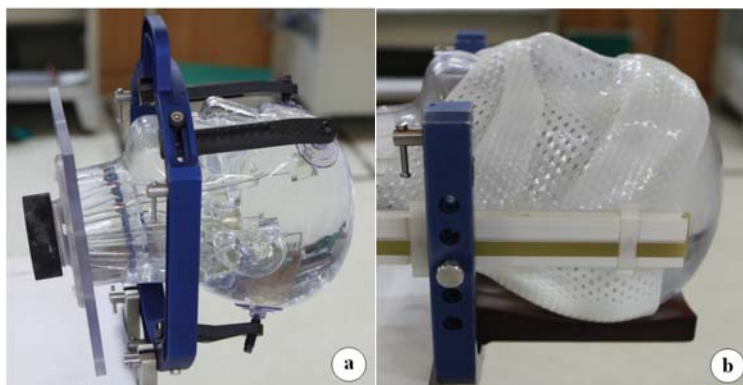


Figure 5A

Figure 5B

Fig. 5. Head phantom setup for virtual treatment. (A, B) Phantom with a BrainLAB[®] head and mask frame for SRS and FSRS treatment, respectively.

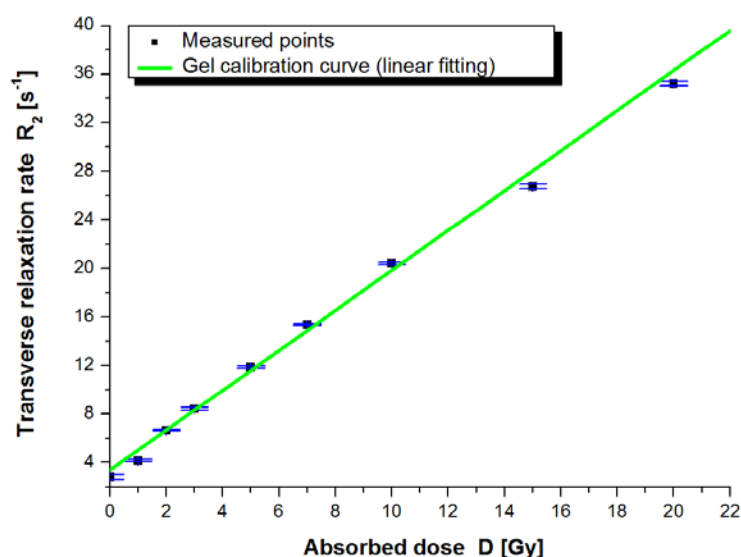


Fig. 6. Calibration curve for polymer-gel dosimeter. All 8 sample vials were subsequently irradiated by 6-MV X-rays using Novalis system. One non-irradiated vial was used for background reading. MR signal was evaluated six times per vial. Linear fitted curve is given $R_2 = 1.646D + 3.391$.

ground readings. Styrofoam[®] (Dow Chemical Co., Michigan, USA) was used for vial immobilization. The same geometry was obtained for each vial using water-equivalent Plastic Water[®] phantom (CNMC Company Inc., Tennessee, USA) and 1.5-cm buildup regions were constructed upward from Styrofoam[®]. Each vial axis was normal to a fixed downward-oriented beam. Each was irradiated in a 4×4 cm² field by 6-MV X-rays using Novalis (BrainLAB, Heimstetten, Germany) at a dose rate of 800 Gy/min.

Virtual treatments using Novalis were simulated using the phantom. Gel-filled vessels were fixed in the water-filled phantom (Figure 5). Then, they were irradiated at 20°C using Novalis for calculated treatment plans. This was repeated thrice for FSRS.

2.5. MRI scan and gel calibration

MRI scans were performed following irradiation

within 30 h using a 1.5-T MAGNETOM[®] Avanto scanner (Siemens, Heidelberg, Germany) at 21°C. For the 9 vials, a spin-echo pulse sequence with repetition time (TR) of 3000 ms and echo times (TEs) of 20 and 100 ms was used. Other scanning parameters were image resolution, 0.47×0.47 mm²; slice thickness, 2.00 mm; and matrix size, 256×256 . For the 10 vessels, MRI scans were performed on the phantom with a transmitter/receiver head coil at the same temperature. The scan parameters differed in that TR was 3300 ms and voxel size, $0.98 \times 0.98 \times 1.00$ mm³. TR for vessels and vials was different. However, T_1 effect could be minimized with TR = 2000–3000 ms [19]. The signal with TR of 3300 ms would not differ noticeably from that of T_2 -weighted MRI images with TR of 3000 ms.

For gel calibration, transverse relaxation rate (R_2) for a specific absorbed dose D with different TE values was determined by [16]

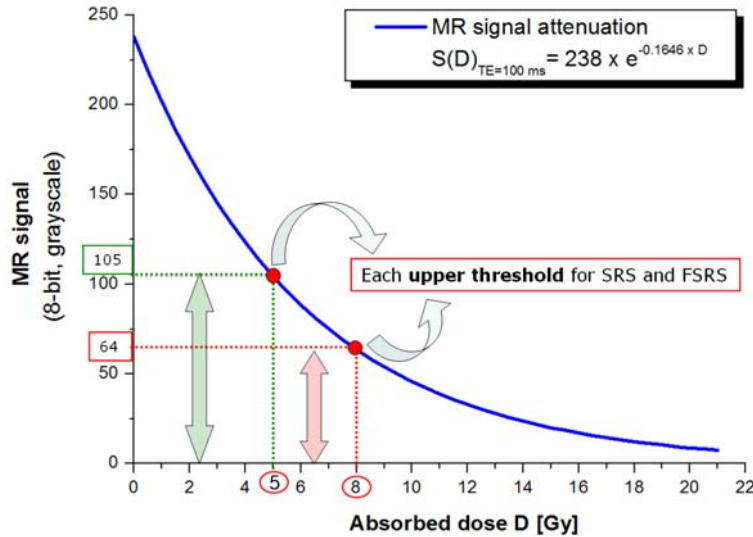


Fig. 7. Monotonic MR signal attenuation graph. Each upper threshold was determined at half the prescribed dose for segmenting each radiation field dyed in the gel dosimeter.

$$S(TE_1) / S(TE_2) = e^{-R_2(D) \times (TE_1 - TE_2)} \quad (1)$$

R_2 was calculated using MATLAB (Ver. 7.11, MathWorks Inc., MA, USA) from $4.70 \times 4.70 \text{ mm}^2$ regions of interest centered in the upper part of the radiation field along each vial axis. A calibration curve of R_2 against absorbed dose was obtained through linear fitting (Figure 6).

2.6. MR signal attenuation and threshold

We define the increasing rate of R_2 with absorbed dose as k and R_2 -axis intercept as α from this graph. The signal in a spin-echo MR image produced by dose D for specific TE is

$$S(TE) = S(0) \times e^{-R_2(D) \times TE} = S'(0) \times e^{-k \times TE \times D}$$

for $S'(0) \equiv S(0) \times e^{-\alpha \times TE}$ (2)

We obtain monotonic exponential graphs for a specific dose range with specific TE with constraint conditions of TE, 100 ms; k , $1.646 \text{ Gy}^{-1} \cdot \text{s}^{-1}$; and $S'(0)_{TE=100 \text{ ms}}$, 238 from the background vial. The graph is expressed as

$$S(D)_{TE=100} = 238 \times e^{-1.646 \times 10^{-1} \times D} \quad (3)$$

We determine the upper signal threshold for segmenting the radiation field. The threshold signal was half the prescribed 100% dose at the isocenter (Figure 7).

2.7. Comparison of analysis methods

The mid bi-plane method analyzes TPDs using the mid bi-plane on a segmented radiation field in the treatment planning system assuming a spherical field. The three-dimensional volume method analyzes a three-dimensional volume as the field shape. To detect the radiation field below pixel values of 64 and 105 for virtual SRS and FSRS treatment analysis, respectively, we modified windowing settings and contoured segmented radiation fields in BrainSCANTM (Figure 8). After selecting each radiation field for the planning target volume, a dummy isocenter positioned at the radiation field center in MR image sets was added. The 10 targets were divided into two groups based on shapes of areas with a planned 50% isodose line (Figure 9) and analysis methods were compared. Targets 1–2 were defined as ellipses and 3–10, as spheres. The radiation field center with both analysis methods for the target groups was compared using

$$\begin{aligned} \Delta AP &\equiv |AP_1 - AP_2| \\ \Delta LAT &\equiv |LAT_1 - LAT_2| \\ \Delta VRT &\equiv |VRT_1 - VRT_2| \end{aligned} \quad (4)$$

$AP_{1/2}$, $LAT_{1/2}$, and $VRT_{1/2}$ are defined as radiation field centers in anterior–posterior (AP), lateral (LAT), and vertical (VRT) directions for the mid bi-plane and three-dimensional volume method, respectively. The difference between the centers is

$$\Delta Total \equiv \sqrt{(\Delta AP)^2 + (\Delta LAT)^2 + (\Delta VRT)^2} \quad (5)$$

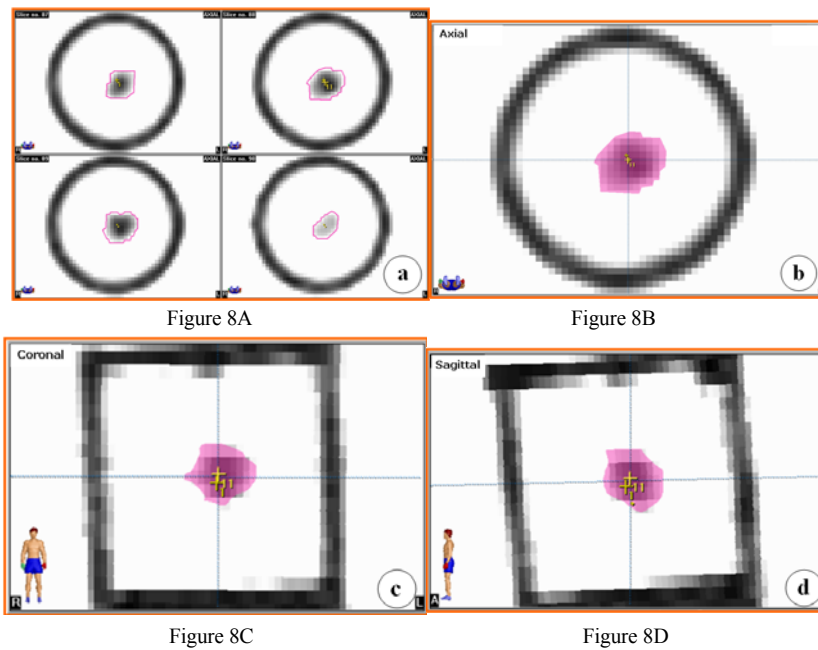


Fig. 8. Contour area of segmented radiation field. Once each upper threshold value has been set in BrainSCANTM, the radiation field area with a 50% isodose level is segmented and determined by contouring the segmented area. (A) Contour of radiation field at each axial slice; (B, C, D) radiation field area for axial, coronal, and sagittal view, respectively.

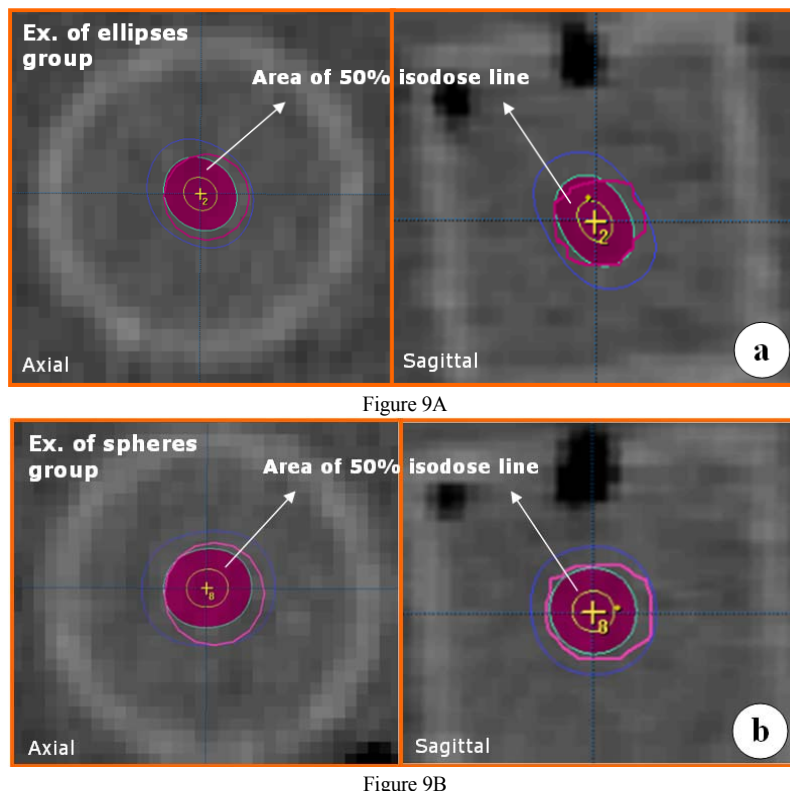


Fig. 9. Example of ellipses and spheres classified by shape of 50% isodose lines in axial and sagittal views. Targets 1 and 2 are defined as ellipses and 3–10, as spheres. (A) Target 2 as an example of ellipses and (B) target 8, as one of spheres.

Consequently, the effect of the analysis method on accuracy for target groups could be determined.

2.8. TPD evaluation

In each treatment, the positions of planned isocenters

in stereotactic coordinates and radiation field centers using three-dimensional volume method were acquired in the same coordinate system. We performed auto-image fusion of CT and MR image sets using BrainSCANTM. Accuracy errors were manually minimized. The differ-

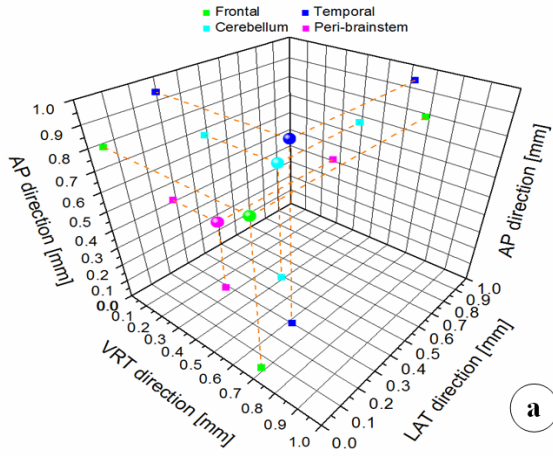


Figure 10A

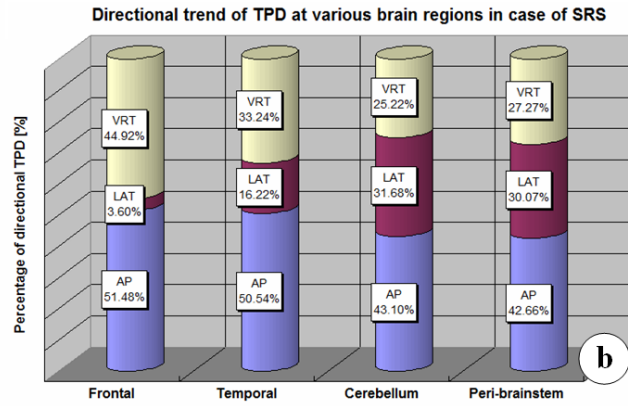


Figure 10B

Fig. 10. Directional TPDs and trends for various brain regions in SRS treatment. (A) Directional TPDs in each region are computed by averaging directional components of targets within that region. (B) TPD_{AP} dominates TPD_{total} for all regions. TPD_{AP} and TPD_{VRT} dominate TPD_{total} in frontal and temporal regions. TPD_{VRT} and TPD_{LAT} contribute similarly to TPD_{total} for cerebellum and peri-brainstem regions.

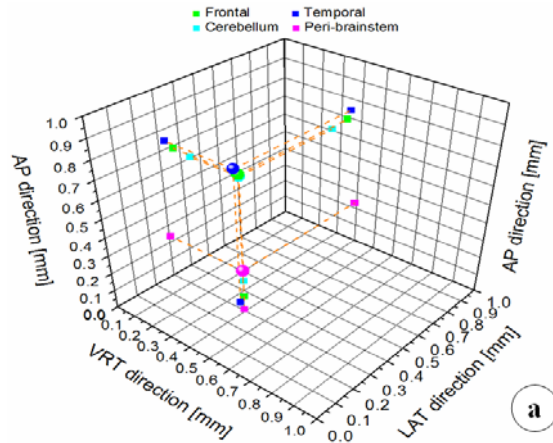


Figure 11A

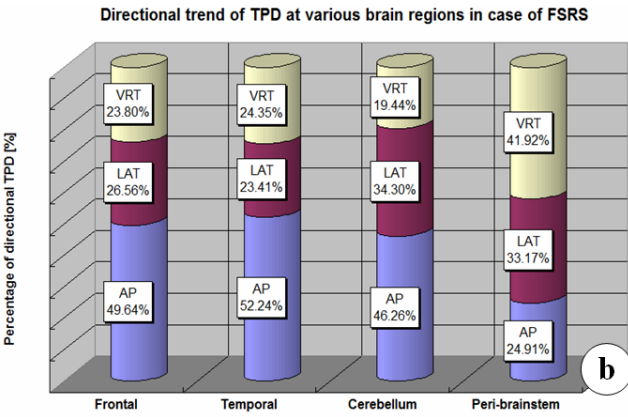


Figure 11B

Fig. 11. Directional TPD and trends for various brain regions in FSRS treatment. (A) Directional TPDs in each region are computed by averaging directional components of targets within that region. (B) TPD_{AP} dominates TPD_{total} in all but the peri-brainstem regions. TPD_{VRT} and TPD_{LAT} contribute similarly to TPD_{total} in frontal and temporal regions. TPD_{AP} and TPD_{LAT} dominate TPD_{total} in the cerebellum region. TPD_{VRT} dominates in the peri-brainstem region.

ence between planned and dummy isocenter positions was used to calculate overall TPD for head and mask frames. Directional TPD was defined as

$$\begin{aligned} TPD_{AP} &\equiv |IP_{AP} - DIP_{AP}| \\ TPD_{LAT} &\equiv |IP_{LAT} - DIP_{LAT}| \\ TPD_{VRT} &\equiv |IP_{VRT} - DIP_{VRT}| \end{aligned} \quad (6)$$

TPD_{AP} , TPD_{LAT} , and TPD_{VRT} denote deviation lengths in AP, LAT, and VRT directions, respectively. The planned (IP) and dummy (DIP) isocenter positions in each direction were defined as IP/DIP_{AP} , IP/DIP_{LAT} , and IP/DIP_{VRT} , respectively. Total TPD was

$$TPD_{total} \equiv \sqrt{(TPD_{AP})^2 + (TPD_{LAT})^2 + (TPD_{VRT})^2} \quad (7)$$

TPD_{total} in frontal, temporal, cerebellum, and peri-brainstem regions was calculated for SRS and FSRS by averaging TPD_{total} for targets within that region. For TPDs in different directions, average directional TPD values of targets within a region were computed to determine directional trends.

3. RESULTS AND DISCUSSION

3.1. Comparison of analysis methods

To determine differences in precision between the two methods, we compared them for the two target groups. Table 1 lists differences between measured positions of radiation field centers for spheres and ellipses.

Expectedly, the difference is larger for ellipses than for spheres. The values indicate that analysis methods affect measured TPDs; the mid bi-plane method causes serious errors for ellipses.

Table 1. Precision of Both Analysis Methods.

Target groups	Difference (mm) (mean \pm standard deviation)	Max. (mm)	Min. (mm)
Ellipses	0.62 ± 0.08	0.69	0.49
Spheres	0.27 ± 0.11	0.46	0.11

3.2. TPD evaluation in various brain regions

To determine directional trends in TPD_{total} in various brain regions, we classified 10 targets by region and calculated average TPD_{total} for the four regions and directional TPDs for each region. Average TPD_{total} at peripheral regions was greater than that at central regions for both treatments.

For virtual SRS, the head frame was used for phantom immobilization. Table 2 lists TPD_{total} for various brain regions. Figure 10A shows directional TPDs for each region. For frontal and temporal regions, TPD_{AP} and TPD_{VRT} dominate. Directional TPDs for cerebellum and peri-brainstem regions are more uniform. Figure 10B shows the contribution of each TPD to TPD_{total} .

Table 2. TPD_{total} for Various Brain Regions in Stereotactic Radiosurgery Treatment.

Region	TPD_{total} (mm) (mean \pm standard deviation)
Frontal	1.04 ± 0.01
Temporal	1.16 ± 0.02
Cerebellum	0.91 ± 0.13
Peri-brainstem	0.56 ± 0.15

Table 3. TPD_{total} for Various Brain Regions in Fractionated Stereotactic Radiosurgery Treatment.

Region	TPD_{total} (mm) (mean \pm standard deviation)
Frontal	0.85 ± 0.11
Temporal	0.90 ± 0.08
Cerebellum	0.80 ± 0.13
Peri-brainstem	0.57 ± 0.10

For virtual FSRS, the mask frame was used for phantom immobilization. Table 3 lists TPD_{total} for various brain regions. The average standard deviation of TPD_{total} is 0.15 mm; the overall setup error of the phantom for three fractionations is therefore ~ 0.15 mm. Figure 11A shows directional TPDs for each region. For frontal, temporal, and cerebellum regions, TPD_{AP} dominates. For peri-brainstem region, TPD_{VRT} dominates. Figure

11B shows the contribution of each TPD to TPD_{total} .

Table 4. TPD Results. Stereotactic Radiosurgery Treatment: Average TPD_{total} , 0.92 ± 0.25 mm; Fractionated Stereotactic Radiosurgery Treatment (three fractionations): Average TPD_{total} , 0.77 ± 0.15 mm.

Displacement direction	TPD (mm) (mean \pm standard deviation)	
	SRS	FSRS
Anterior-posterior	0.70 ± 0.25	0.54 ± 0.23
Lateral	0.28 ± 0.22	0.37 ± 0.08
Vertical	0.49 ± 0.25	0.33 ± 0.10
Total	0.92 ± 0.25	0.77 ± 0.15

For both SRS and FSRS cases, the results can not be examined with specific factor because it was measured without step by step measurement during treatment. Although it was detected step by step, we were not able to analyze it because the results always generated by randomly combination of specific erroneous factors. On the other hand, if the data has same trend of TPD through repetition, it can be used for assigning extra irregular margin from CTV (clinical target volume) to PTV (planning target volume).

Table 4 summarizes TPD results. These data apparently provide an incorrect estimate because virtual treatments are performed using a rigid phantom; real patients can move. Without self-motion, mask frames are superior to head frames because the higher-friction surface encloses the phantom compactly. Therefore, in actual FSRS, average TPD_{total} is >0.77 mm and likely exceeds or approximates 1.00 mm for both average TPD_{total} and its standard deviation.

3.3. Comprehensive summary and meaning of the TPD results

To determine the precision of the radiosurgical system, the whole treatment procedure must be simulated. However, QA-related reports have focused on the accuracy of only certain aspects, such as 3D-imaging devices [20–22], dose calculation and dosimetry [23–27], and mechanical accuracy of system [28–30], and not all.

Tests of each treatment step indicate that radiological precision of treatment units and distortion during image processing mainly affect treatment. Deviations during irradiation using a LINAC-based system can be caused by mechanical isocenter errors $e_{mechanical}$, patient setup errors caused by adjustments to target points on stereotactic localizer to isocenter e_{setup} , and immobilization errors in a frame e_{frame} . $e_{frame} = 0.4 \pm 0.3$ and 0.7 ± 0.5 mm were obtained using a BRW stereotactic head frame and BrainLAB[®] mask frame with an image-guidance system, respectively [31]. Studies on deviations in treatment

units reported $e_{\text{mechanical}} < 1.00$ mm, sub-millimeter eframe with an invasive head frame, and $e_{\text{frame}} = 2.00 \pm 1.00$ mm with a thermoplastic mask frame without positive or negative directions; $e_{\text{setup}} = 0.20 \pm 0.10$ mm was obtained using wall and ceiling lasers [9,29,30,32–35].

Other errors are introduced by MR image distortion and image fusion. Mean MR distortion was verified as 1.4 ± 0.4 mm with voxel size of $1.10 \times 1.10 \times 3.30$ mm³ [36], and as 0.72 ± 0.20 mm toward the temporal bone with voxel size of $0.86 \times 0.98 \times 2.00$ mm³ [13]. On the other hand, mean spatial errors because of MR imaging and auto-image fusion with similar voxel sizes as we used were 0.22 ± 0.10 and 0.41 ± 0.30 mm, respectively; spatial errors were mainly caused by image fusion, along with mechanical errors caused by gantry and couch wobble [35].

Studies have focused on overall accuracy resulting from image distortions, target localization and definition, dose calculation, biological model, patient positioning, and mechanical accuracy [10–13,37]. Rosenzweig et al. emphasized QA for all treatment steps [37]. Ertl et al. used the unknown targeting method to verify spatial deviation between irradiated and planned targets [13]. Mack et al. found that a 3D-MPR sequence is superior to T1-weighted spin-echo sequences in terms of overall target point accuracy [12].

Global system tests can evaluate overall effects of all treatment steps. The whole treatment procedure can be simulated [9]. Test targets need to be located at unknown positions inside a phantom to simulate real treatment. The accuracy includes errors from all treatment steps.

Our TPD_{total} values are relatively larger than those of other hidden target tests [10–13]. However, comparisons are difficult because of differences in analysis methods, treatment machines, and support units; also, most studies measured TPD_{total} in only one region at the center of the phantom.

Most studies [10–13,37] on overall spatial accuracy of SRS used two orthogonal square pieces of radiochromic film, corresponding to various orientations. These films were carefully aligned in a rigid phantom. After simulated irradiation, they were digitized and analyzed to quantify the deviation between radiation field center and planned isocenter positions. However, these tests involve serious problems. The first is assuming a spherical radiation field. One can be created if mechanical errors originating from gantry and couch rotation are absent or negligible, and all combinations of gantry and couch angles are used during treatment. This is unlikely because 0.5–0.7-mm mechanical isocenter deviation

is present in all LINAC-based systems because of gantry sag and axis procession of gantry and couch [9], and a limited combination of angles is used to protect OARs in real treatments; this causes the radiation field to become elliptical. We require TPDs based on a field created using a combination of angles used in actual situations and by considering mechanical errors. Therefore, the field is more elliptical than spherical, as mentioned above.

Most global hidden target tests have only one bi-planar film fixed at the center of a head phantom [10–12] because using several bi-planes is laborious. TPDs cannot be simultaneously analyzed at various brain regions using this setup. Our phantom can simultaneously provide information about regional TPDs in various regions. We used a single commercial treatment planning program. We used MATLAB for gel calibration; Image J (National Institute of Mental Health, Maryland, USA) and a calculator can also be used.

Therefore, our analysis method does not suffer from the abovementioned limitations.

However, it has some disadvantages. It relies on the auto-image fusion accuracy, the geometric error of which is 0.41 ± 0.30 mm in BrainSCANTM with CT and MR image sets [35]. The image conditions were 512×512 and 256×256 matrix and 1-mm slice thickness for these respective sets. We obtained better image fusion accuracy because the 0.33-mm slice thickness in CT images is more precise; we used the above-mentioned matrix conditions and manually minimized additional errors.

MR image acquisition time is rather long. 23 min were required to scan the phantom once with a T_2 -weighted spin-echo sequence and voxel size of $0.98 \times 0.98 \times 1.00$ mm³, because we used voxel size of $1 \times 1 \times 1$ mm³ to minimize unnecessary errors caused by the resolution of MR sets. To reduce the time, fast scanning techniques such as turbo spin-echo and fast gradient-echo must be investigated.

We did not measure R_2 -dose response from each gel batch, but calculated a gel calibration curve for one batch. This can change some upper threshold values at doses of 5 and 8 Gy; however, the BANGkitTM reproducibility is stable for 0–12 Gy with a standard deviation of $0.06 \text{ Gy}^{-1} \cdot \text{s}^{-1}$ about the increasing rate in R_2 -dose calibration curves [18]. The threshold value can thus change by ± 3 . This generates relative maximum errors of 4.81% for SRS and 3.00% for FSRS. The inherent precision of TPD results for FSRS is thus probably relatively superior because gray values are higher in the low- than in the high-dose region in the MR signal attenuation graph.

Additional analysis errors can be caused by contouring the radiation field area. To quantify this, we conducted intra- and inter-personal error tests. For the former, one person measured the dummy isocenter position five times after contouring the radiation field for all 10 targets. Standard deviation was 0.12 mm. We compared measured dummy isocenter positions obtained by two people to determine the inter-personal error. The average difference was 0.15 mm and standard deviation, 0.06 mm. Test results indicate a negligible additional error because of contouring relative to those caused by image fusion accuracy or MRI image resolution.

In addition, there is a doubt whether sub-millimeter TPD values measured from voxel size of $0.98 \times 0.98 \times 1.00 \text{ mm}^3$ are credible. This concern can be solved by using error propagation theory that is able to expect the uncertainty calculated from various values with uncertainty. By using the uncertainty of $0.98 \times 0.98 \times 1.00 \text{ mm}^3$ and the average value volume of radiation field of 0.15 cm^3 , the uncertainty of center of radiation field value has about 0.09 mm along the each axis. This means that the measured TPD data can be trusted at least to first places for decimals.

Consequently, although our analysis technique relies on image fusion accuracy and scan parameters, studies to improve MR resolution, image fusion accuracy between CT and MR image sets, and fast MR scanning techniques will enable fast and more exact TPD detection.

4. CONCLUSIONS

Average total TPD is within previously reported error ranges. However, at peripheral regions, it tends to be larger than that at central regions, and may be less than that assumed for high-precision stereotactic treatment, i.e., maximum deviation <1 mm. Our gel-dosimetry-based three-dimensional volume method allows real three-dimensional quantification of overall TPDs for both spheres and ellipses. We show that the mid bi-plane method generates unnecessary errors, assuming a spherical radiation field. Overall system analysis is easy because our technique requires only analysis software provided in the treatment planning system. Therefore, our technique could be used as an overall system accuracy test that easily considers the real radiation field shape.

ACKNOWLEDGMENTS

This work was supported by the National Research Foundation of Korea (Grant No. 2010-008144, BAERI, NRF, MEST).

REFERENCES

1. Likhterov I, Allbright RM, Selesnick SH. LINAC radiosurgery and radiotherapy treatment of acoustic neuromas. *Neurosurg. Clin. North Am.* 2008;19:345-365.
2. Müller-Riemenschneider F, Bockelbrink A, Ernst I, Schwarzbach C, Vauth C, Schulenburg J, Willich S. Stereotactic radiosurgery for the treatment of brain metastases. *Radiother. Oncol.* 2009;91:67-74.
3. Sun DQ, Carson KA, Raza SM, Batra S, Kleinberg LR, Lim M, Huang J, Riquamonti D. The radio-surgical treatment of arteriovenous malformations: Obliteration, morbidities, and performance status. *Int. J. Radiat. Oncol. Biol. Phys.* 2010;1-8 (Article in Press).
4. Flickinger JC, Schell MC, Larson, DA. Estimation of complications for linear accelerator radiosurgery with the integrated logistic formula. *Int. J. Radiat. Oncol. Biol. Phys.* 1990;19:143-148.
5. Heifetz MD, Whiting J, Bernstein H, Wexler M, Rosemark P, Thomson RW. Stereotactic radiosurgery for fractionated radiation: A proposal applicable to linear accelerator and proton beam programs. *Stereotact. Funct. Neurosurg.* 1989;53:167-177.
6. Souhami L, Olivier A, Podgorsak EB, Villemure JG, Pla M, Sadikot A. Fractionated stereotactic radiation therapy for intracranial tumors. *Cancer* 1991;68:2101-2108.
7. Ramaseshan R, Heydarian M. Comprehensive quality assurance for stereotactic radiosurgery treatments. *Phys. Med. Biol.* 2003;48:199-205.
8. Klein EE, Hanley J, Bayouth J, Yin F, Simon W, Dresser S, Serago C, Aguirre F, Ma L, Arjomandy B, Liu C. Task Group 142 report: Quality assurance of medical accelerators. *Med. Phys.* 2009;36:4197-4212.
9. Schell MC, Bova FJ, Larson DA, Leavitt DD, Lutz WR, Podgorsak EB, Wu A. Task Group 42 report: Stereotactic radiosurgery. American Association of Physicists in Medicine. American Institute of Physics 1995.
10. Feygelman V, Walker L, Chinnaiyan P, Forster K. Simulation of intrafraction motion and overall geometric accuracy of a frameless intracranial radiosurgery process. *J. Appl. Clin. Med. Phys.* 2008;9:68-86.
11. Mack A, Mack G, Scheib S, Czempiel H, Kreiner HJ, Lomax NJ, Gianolini S, Rieker M, Weltz D, Wolff R, Muacevic A, Wowra B, Bottcher HD, Seifert V. Quality assurance in stereotactic radiosurgery/radiotherapy according to DIN 6875-1.

- Stereotact. Funct. Neurosurg. 2004;82:235-243.
12. Mack A, Czempel H, Kreiner H-J, Durr G, Wowra B. Quality assurance in stereotactic space. A system test for verifying the accuracy of aim in radiosurgery. *Med. Phys.* 2002;29:561-568.
 13. Ertl A, Saringer W, Heimberger K, Kindl P. Quality assurance for the Leksell gamma unit: Considering magnetic resonance image-distortion and delineation failure in the targeting of the internal auditory canal. *Med. Phys.* 1999;26:166-170.
 14. Semnicka J, Novonty J, Spevacek V, Garcic J, Steiner M, Judas L. Three-dimensional gel dosimetry for dose volume histogram verification in stereotactic radiosurgery. *Radiosurgery* 2010;7:44-55.
 15. Sandilos P, Tatsis E, Vlachos L, Dardoufas C, Karaiskos P, Georgiou E, Baras P, Kipourous P, Torrens M, Angelopoulos A. Mechanical and dose delivery accuracy evaluation in radiosurgery using polymer gels. *J. Appl. Clin. Med. Phys.* 2006;7:13-21.
 16. Maryanski MJ, Schulz RJ, Ibbott GS, Gatenby JC, Xie J, Horton D, Gore JC. Magnetic resonance imaging of radiation dose distributions using a polymer-gel dosimeter. *Phys. Med. Biol.* 1994;39:1437-1455.
 17. Baldock C, De Deene Y, Doran S, Ibbott G, Jirasek A, Lepage M, McAuley KB, Oldham M, Schreiner LJ. Polymer gel dosimetry. *Phys. Med. Biol.* 2010;55:R1-R63.
 18. Murakami Y, Nakashima T, Watanabe Y, Akimitsu T, Matsuura K, Kenjo M, Kaneyasu Y, Wadasaki K, Hirokawa Y, Ito K. Evaluation of the basic properties of the BANGkitTM gel dosimeter. *Phys. Med. Biol.* 2007;52:2301-2311.
 19. Hashemi RH, Bradley Jr. WG, Lisanti CJ. MRI: The basics. 2nd ed. Lippincott Williams & Wilkins; 2004:49-57.
 20. Barker GJ, Tofts PS. Semiautomated quality assurance for quantitative magnetic resonance imaging. *Magn. Res. Imaging.* 1992;10:585-595.
 21. Mutic S, Palta JR, Butker EK, Das I, Huq M, Loo L, Salter B, McCollough C, Dyk J. Quality assurance for computed-tomography simulators and the computed-tomography-simulation process: Report of the AAPM Radiation Therapy Committee Task Group No. 66. *Med. Phys.* 2003;30:2762-2792.
 22. Bissonnette J-P. Quality assurance of image-guidance technologies. *Semin. Radiat. Oncol.* 2007;17:278-286.
 23. Petrovic B, Grzadiel A, Slosarek K. Quality assurance of TPS: Comparison of dose calculation for stereotactic patients in Eclipse and iPlan RT Dose. *Rep. Pract. Oncol. Radiother.* 2009;14:5-10.
 24. Duggan DM, Coffey II CW. Small photon field dosimetry for stereotactic radiosurgery. *Med. Dosim.* 1998;23:153-159.
 25. Lee KY, Karl KLF, Kwok CS. Application of high-resolution radiochromic film dosimetry in verifying a small-field stereotactic radiosurgery plan. *Appl. Radiat. Isot.* 2006;64:934-939.
 26. Massillon-JL G, Minniti R, Soares CG, Maryanski M, Robertson S. Characteristics of a new polymer gel for high-dose gradient dosimetry using a micro optical CT scanner. *Appl. Radiat. Isot.* 2010;68:144-154.
 27. Kabat D, Nahajowski D, Gora E, Bogusz B, Lesiak J, Polak B, Czopyk L, Olko P, Walligorski M. On the clinical application of large-area 2-D TL dosimetry for verifying small photon radiotherapy beams. *Radiat. Meas.* 2008;43:1004-1007.
 28. Van Dam J, Johansson K-A, Bridier A, Sernbo G, Hansson U. EORTC radiotherapy group quality assurance: Mechanical checks and beam alignments of megavoltage equipment. *Radiother. Oncol.* 1993;29:91-96.
 29. Tsai J-S, Curran BH, Sternick ES, Engler M. The measurements of linear accelerator isocenter motion using a three-micrometer device and an adjustable pointer. *Int. J. Radiat. Oncol. Biol. Phys.* 1996;34:189-195.
 30. Gibbs Jr. FA, Buechler D, Leavitt DD, Moeller J. Measurement of mechanical accuracy of isocenter in conventional linear accelerator-based radiosurgery. *Int. J. Radiat. Oncol. Biol. Phys.* 1993;25:117-122.
 31. Ramakrishna N, Rosca D, Friesen S, Tezcanli E, Zyqmanski P, Hacker F. A clinical comparison of patient setup and intra-fraction motion using frame-based radiosurgery versus a frameless image-guided radiosurgery system for intracranial lesions. *Radiother. Oncol.* 2010;95:109-115.
 32. Friedman WA, Bova FJ. The University of Florida Radiosurgery System. *Surg. Neurol.* 1989;32:334-342.
 33. Karger CP, Jakel O, Debus J, Kuhn S, Hartmann G. Three-dimensional accuracy and interfractional reproducibility of patient fixation and positioning using a stereotactic head mask system. *Int. J. Radiat. Oncol. Biol. Phys.* 2001;49:1493-1504.
 34. Willner J, Flentje M, Bratengeier K. CT simulation in stereotactic brain radiotherapy – analysis of isocenter reproducibility with mask frame. *Radiother. Oncol.* 1997;45:83-88.
 35. Rahimian J, Chen JC, Rao AA, Girviquian MR,

- Miller MJ, Greathouse HE. Geometrical accuracy of the Novalis stereotactic radiosurgery system for trigeminal neuralgia. *J. Neurosurg.* 2004;101:351-355.
36. Karger CP, Hoss A, Bendl R, Canda V, Schad L. Accuracy of device-specific 2D and 3D image distortion correction algorithms for magnetic resonance imaging of the head provided by a manufacturer. *Phys. Med. Biol.* 2006;51:N253-N261.
37. Rosenzweig DP, Schell MC, Numaguchi Y. Quality assurance in Linac-based stereotactic radiosurgery and radiotherapy. *Med. Dosim.* 1998;23:147-151.